ORIGINAL ARTICLE

lajss.org Latin American Journal of Solids and Structures

www.lajss.org

Simplified Approach for Assessing the Explosive Residual Strength of Ship Hulls

Jiaxin Wu[a], Ming Yan[a*], Xingwei Sun[a]

[a]Liaoning Shock Protection and Damage Assessment Technology Engineering Research Center, Shenyang University of Technology, Shenyang, China. Email: wujiaxin@smail.sut.edu.cn, yanming7802@163.com, sunxingw@126.com

*Corresponding author

https://doi.org/10.1590/1679-78258339

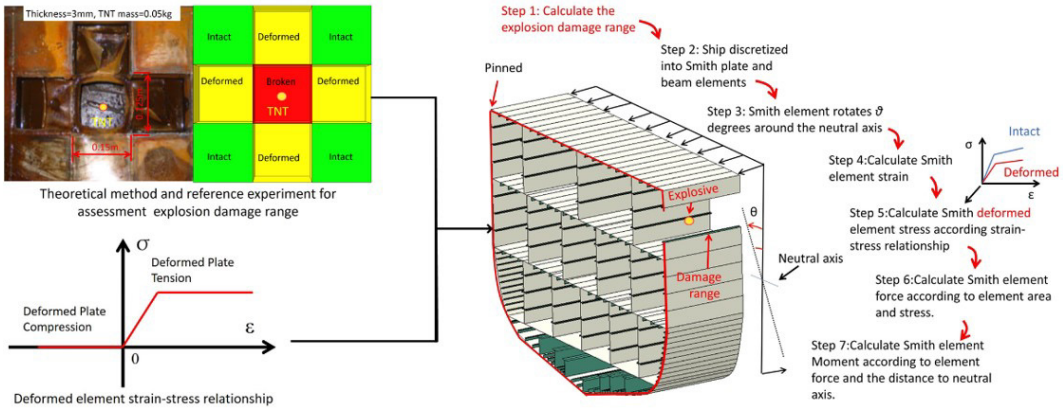
Abstract

To evaluate the residual strength of the ship after explosion, the Explosion Smith Method (ESM) is proposed. The innovation of the ESM lies in two aspects: firstly, based on the Baker shock wave and quasi-static pressure model, Jones critical velocity model, propose a method for assessing the range of explosion damage of cabin and validated through referenced experiments. Secondly, proposes the strain-stress relationship of the deformation element. To verify the feasibility of the ESM and study the influence of TNT location and mass,16 simulations and EMS calculations were conducted. The results showed that the residual strength is most impacted when the TNT in top deck. For side cabin, the explosion products discharged and impact reduced. The trend of the ESM and simulation were consistent, but the result of ESM was more severe. The reason that strain-stress relationship of the deformation element more stringent, resulting in the ESM smaller than the simulation. However, as the TNT increases the error decreases. In the future, more research can be conducted on the deformed structures to enhance the accuracy of the ESM.

Keywords

Residual Strength, Ultimate Strength, Explosion, Explosion Smith method, Smith method, Evaluation methodology, Damage assessment method.

Graphical Abstract



Received August 14, 2024. In revised form September 02, 2024. Accepted September 02, 2024. Available online September 04, 2024.
https://doi.org/10.1590/1679-78258339

Latin American Journal of Solids and Structures. ISSN 1679-7825. Copyright © 2024. This is an Open Access article distributed under the terms of the Creative Commons Attribution License, which permits unrestricted use, distribution, and reproduction in any medium, provided the original work is properly cited.

1 INTRODUCTION

Ships are vital for trade and transportation, so ensuring and enhancing hull safety is crucial for their secure operation. In recent years, ships in the Red Sea have experienced a series of attacks, resulting in significant economic and property losses, highlighting the importance of researching structural damage caused by explosions. On January 27, 2024, CNN reporter Anna (2024) reported on the fire accident of the Marin Luanda oil tanker after it was attacked in the Gulf of Aden in the Red Sea. Norman (2024) from Foxnews reported that the RubyMar cargo ship was hit and sunk by a missile while sailing in the same area on March 3, 2024. Moreover, as shown in Figure 1, On July 15, 2024, Jaidaa (2024) from MarineLink reported that the oil tanker Hios Lion was attacked in the Red Sea. Before discussing ship explosions and fire accidents, let's introduce a worth referencing case. According to the EMSA (European Maritime Safety Agency) data (2024) shows that collisions caused the most severe casualties in 2014 and 2017, resulting in 48 and 74 casualties, respectively. Many scholars, including Prabowo (2017), Calle (2017) and Martinez (2020), provided very important references for the study of residual strength after frequent ship collisions. Scholars' continuous efforts have gradually reduced the number of casualties caused by collisions since 2017, which is a great achievement. Similarly, like the casualties of ship collisions in 2014 and 2017, the EMSA data in Figure 2 also indicate a rise in explosion and fire fatalities from 2020 to 2022, with an unusually high rate of fire and explosion in 2022. Although the number of explosion and fire accidents was not specifically mentioned, from the perspective of casualties, explosion and fire accidents are showing a potential increasing trend. Additionally, the explosion not only causes casualties to individuals, but also damages the ship's hull, and residual strength is a crucial indicator for evaluating the ultimate bearing capacity of the hull after damage. Therefore, similar to the case of reducing casualties in ship collision research, evaluating the residual strength quickly and reasonably after an explosion is of great significance in ship design, manufacturing, optimization, and emergency rescue areas, particularly because of the potential and increasing frequency of explosion accidents.



Figure 1 The Chios Lion oil tanker was attacked in the Red Sea.

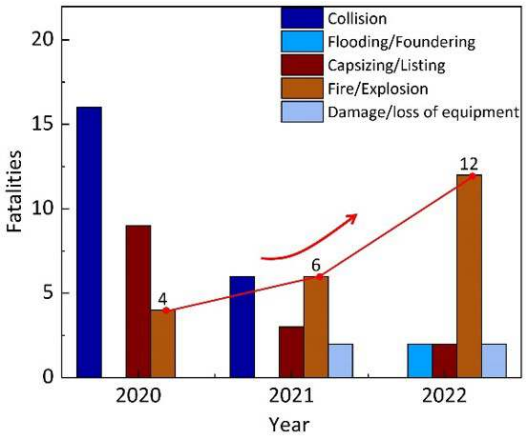


Figure 2 EMO data shows a rapid increase in casualties caused by fires/explosions.

The economic losses resulting from numerous explosion accidents, along with the pollution caused by sinking ships, have gradually drawn the attention of scholars. To evaluate the destructive effect of explosions on hulls and improve their residual strength, scholars have conducted extensive research. Li et al. (2022) performed explosion simulations on typical steel box structures found on ships and put forward a technique for promptly estimate the level of damage to steel box structures when exposed to internal explosion loads. Li conducted dimensionless analysis on the factors influencing the strength of steel box structures. In addition, Li uncovered that the damage modes resulting from explosions can be classified as follows: significant plastic deformation, central fracture, tearing at corners or edges, and shear damage. Wu et al. (2018) used numerical simulation methods to compare the structural deformation and residual strength of ship compartments with box girder structures and conventional structures of equal weight under internal explosion loads. The results showed that the box girder structure significantly improves the residual strength of the ship without increasing the cross-sectional area of the longitudinal components of the main hull, with the improvement effect related to the location of the explosion point. Xu et al. (2019) studied the residual strength of the damaged and deformed portion of the strong deck under air explosion conditions, fitting the deck's deformation curve using trigonometric series. Qiao et al. (2017) applied the CONWEP method to simulate the dynamic structural response of a typical three-compartment ship model under varying explosion locations and masses. By utilizing quasi-static loading methods, Qiao introduced a new impact factor based on structural shielding explosion energy. This new factor, which accounts for the explosion's mass, location, and the affected structural area, provides a better representation of the overall structural damage from explosion loads compared to traditional shock factors based on explosion wave overpressure. Arora et al. (2014) evaluate the residual strength of composite sandwich panels which potential using in ship hull, and following an explosion impact, with a particular focus on the structural performance after explosion-induced damage. Research indicates that CFRP sandwich panels demonstrate lower maximum displacement than GFRP sandwich panels under explosive impacts, suggesting that CFRP offers superior blast resistance. Cerik (2018) studied the impact of large plastic deformation due to lateral local loads on the longitudinal compression behavior of steel plates from ship hull. Research has shown that damage from lateral local loads affects not only the residual strength of steel plates but also their entire load-shortening response range under uniaxial longitudinal compression. Khalifa (2015) investigated the damage mode caused by explosions to submerged structures in enclosed environments, and evaluated the dynamic response of lightweight cold-formed steel sandwich panels under explosive loads through experiments, including their tensile and compressive properties. Yao et al. (2023) investigated the dynamic response and failure of large multi-box steel structures, which are typical structural components of ships, subjected to internal explosion loads through experimental research. Detailed damage characteristics of the dynamic response process of the central section, main transverse partition, and overall model were described, and improvement suggestions for multi-box structural design were proposed. Smith et al. (2003) established a hypothetical scenario of explosion damage range for HALIFAX class ships, where the explosion occurred in the middle of the starboard side of the main deck. Through the ULTSAS program, it was found that the preset explosion range resulted in a reduction of 18% in sagging strength and 11% in hogging strength during vertical bending. Mantena et al. (2010) conducted research on explosion and impact resistant composite panels for naval vessels and investigated the residual strength of various composite panels after explosions. The study revealed that the TYCOR core material is lighter and possesses a higher strength. Sun et al. (2006) analyzed the plastic deformation of damaged ships caused by non-contact explosions and found that, while keeping other parameters constant, the maximum plastic strain and maximum deformation of the cargo hold structure are inversely proportional to the explosion distance. When the load increases to a certain value, the shell plate collapses earlier than the frame beam. Leelachai et al. (2015) simplified the explosion damage area into circular holes and analyzed the impact of holes with different areas on the residual strength. The results indicate that the residual strength is inversely proportional to the size of the damaged area.

An analysis of the aforementioned research indicates that current methods for assessing the residual strength of ships under internal explosion conditions primarily depend on experimental and simulation, lacking theoretical evaluation approaches. These simulation and experimental methods have lengthy cycles and require specialized ex-perimental and technical conditions, making them less suitable for rapid evaluation of the residual strength of ships in explosion scenarios. Bhardwaj et al. (2021) proposed a method for quantifying the risk of FPSO fires and explosions, emphasizing that risk assessment is an effective decision-making tool for preventing, mitigating, and recovering from potential accidents. Therefore, to quickly evaluate the residual strength of ships under explosion conditions and provide decision-making support for rescue operations, a theoretical evaluation method called the explosion Smith method is proposed.

2 Materials and Methods

Before introducing the explosion Smith method, let's briefly introduce the Smith method. The Smith method is developed by Smith (1977), it is widely used for evaluating the ultimate strength of ship hulls. As shown in Figure 3, the

calculation is divided into 6 steps. Step 1 is to discretize the ship structure into Smith plate elements and beam elements. Step 2, rotate all elements around the neutral axis by an angle θ. Step 3, calculate the strain of each element. Step 4, determine the stress value based on the strain-stress relationship of the element. Step 5, calculate the force on the element based on the stress and element area. Step 6, calculate the moment of the element based on the force and the distance between the element and the neutral axis. By continuously increasing the curvature value and repeating the above steps, the ultimate strength of the ship can be calculated.

It can be easily observed that the Smith method mainly faces two challenges when evaluating the residual strength of explosive ship hulls. The first one is that the Smith method cannot calculate the range of damage caused to the ship's hull by an explosion. The second one is that the ship undergoes deformation after the explosion, and the Smith method lacks the strain-stress relationship of the element under deformation conditions.

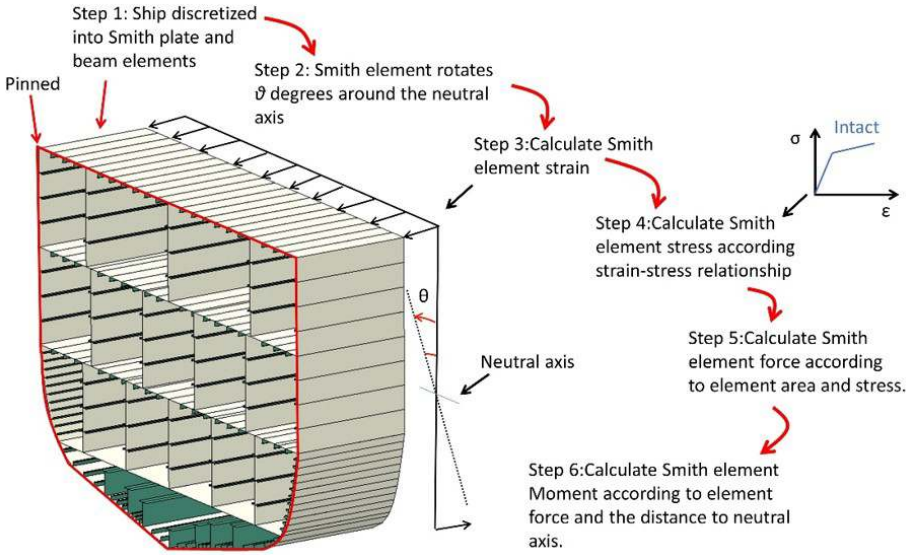


Figure 3 Schematic diagram of the calculation process of Smith method.

To address these two issues, the first point in sections 2.1-2.5 is to propose an evaluation method for assessing the range of explosion damage and validate it using experiments from the reference literature. The second point is to propose a strain-stress relationship for the deformed Smith element in section 2.6. Based on the above two points, the explosion Smith method is proposed in section 2.7. The calculation process of the explosion Smith method is shown in Figure 4.

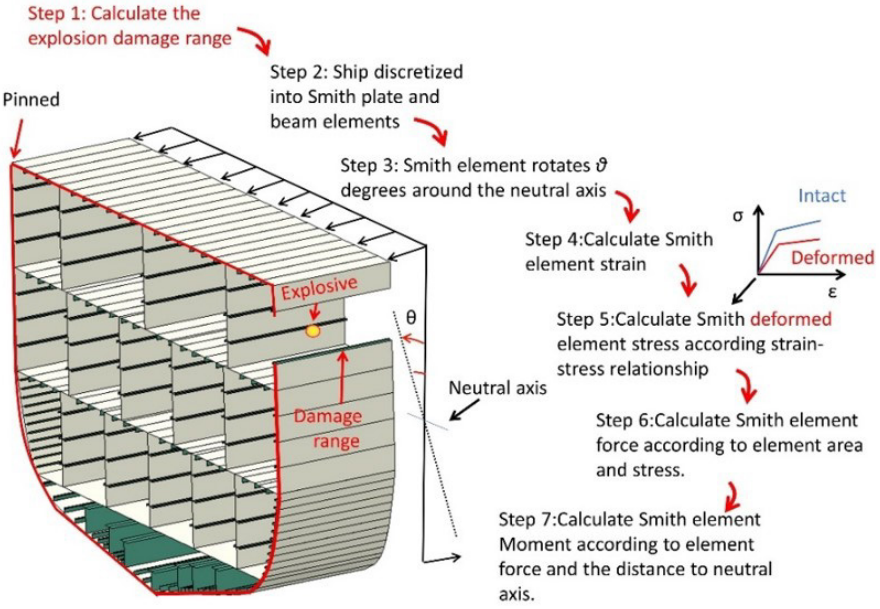


Figure 4 Schematic diagram of the calculation process of explosion Smith method.

2.1 Simplification of load in explosion chamber

Figure 5 shows the cabin model explosion test conducted in the United States as mentioned by Lee et al. (2015). Beshara (1994) measured the time history curve of the pressure on the inner wall during the explosion, as shown in Figure 6, and found that it can be divided into two stages based on the type of shock wave: the shock wave pressure stage and the quasi-static pressure stage. Baker et al. (1983) proposed a simplified explosion pressure model for both the shock wave stage and the quasi-static pressure stage.



Figure 5 Cabin explosion test.

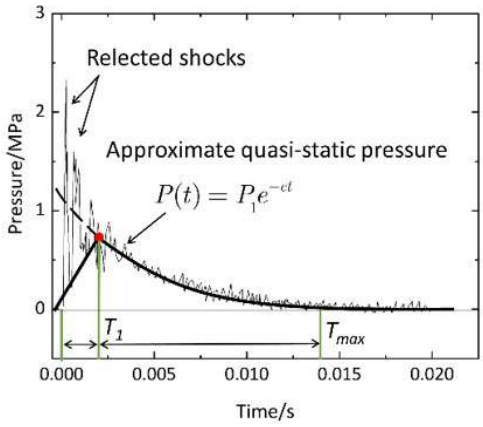


Figure 6 Beshara measured the typical pressure-time curve of an explosion's inner wall.

In Baker's analysis of the typical shock wave curve, as depicted in Figure 7, it is noted that during the shock wave stage, Baker accounts for the first three shock waves. Baker adjusts the peak values such that the second shock wave's peak is halved, and the peak of the third shock wave is halved once more. Regarding the duration of the shock waves, it is assumed that all three shock waves last the same amount of time, denoted as T_{R1}=T_{R2}=T_{R3}, and it is posited that T_R equals $2T_a$. From Figure 7, the total duration of the shock wave stage T_1=$3T_R$=$6T_a$.

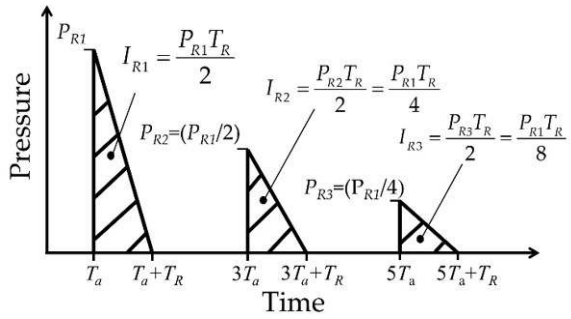


Figure 7 Baker simplified explosion load model.

In Figure 7, Wang (2021) used the peak incident shock wave pressure Δ*P* is calculated using the empirical equation (1) proposed by Henrych.

$$\Delta P = \begin{cases} \dfrac{1.40717}{Z} + \dfrac{0.55397}{Z^2} - \dfrac{0.03572}{Z^3} + \dfrac{0.000625}{Z^4} & 0.05 \le Z \le 0.3 \\ \dfrac{0.61938}{Z} - \dfrac{0.03262}{Z^2} + \dfrac{0.21324}{Z^3} & 0.3 \le Z \le 1 \\ \dfrac{0.0062}{Z} + \dfrac{0.405}{Z^2} + \dfrac{0.3288}{Z^3} & 1 \le Z \le 10 \end{cases} \tag{1}$$

Where *Z* represents the proportional distance, $Z = \dfrac{R}{\sqrt[3]{W}}$, *R* denotes the burst distance, and *W* signifies the masses of TNT.

In order to calculate the pressure on the cabin wall, establish a cartesian coordinate system for the target bulkhead, and set the center of the bulkhead as the origin (0,0,0). The projection distance from the TNT to the target bulkhead is *l*, as shown in Figure 8. The distance from any point on the bulkhead to the explosion point l_i is given by the equation (2).

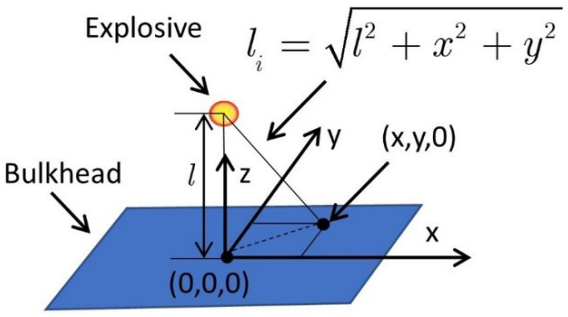


Figure 8 Schematic diagram of the distance between the explosive and any point on the bulkhead.

$$l_i = \sqrt{l^2 + x^2 + y^2} \tag{2}$$

The angle of the incident wave *φ*, was calculated using equation (3):

$$\varphi = \arccos \frac{l}{\sqrt{l^2 + x^2 + y^2}} \tag{3}$$

The peak value of the reflected shock wave, P_R is calculated using equation (4):

$$P_R = \left[\left(1 + \cos\varphi\right)\Delta P + \frac{6\Delta P^2}{\Delta P + 7P_0} \cos^2 \varphi \right] \tag{4}$$

In equation (4), P_0 represents the atmospheric pressure, which is P_0=101325Pa.

Based on the explosion test results by Henrych, an empirical equation for the duration of the positive pressure phase of the shock wave, denoted as T_R, is proposed in equation (5):

$$T_R = \left(0.107 + 0.444Z + 0.264Z^2 - 0.129Z^3 + 0.0335Z^4\right)\sqrt[3]{W} \tag{5}$$

The impulse I_S caused by the three shock waves is calculated using equation (6):

$$I_S = I_{R1} + I_{R2} + I_{R3} = \frac{P_{R1}T_R}{2} + \frac{P_{R2}T_R}{2} + \frac{P_{R3}T_R}{2} = \frac{P_{R1}T_R}{2} + \frac{P_{R1}T_R}{4} + \frac{P_{R1}T_R}{8} \tag{6}$$

From Figure 6, it is observable that the peak quasi-static pressure in a confined local space during an explosion follows the attenuation of the shock wave to quasi-static pressure. In Figure 9 illustrates that Baker introduced an approximate equation for quasi-static pressure, referenced as equation (7), and contended that the period before T_1 represents the shock wave phase, with the quasi-static pressure developing thereafter. It is expected to rise from zero, reaching its peak at point A, and then decline exponentially to the atmospheric pressure P_0. Therefore, the point P_{Qmax} is identified as the peak quasi-static pressure during an explosion when a venting port is present.

$$P\left(t\right) = P_1 \mathrm{e}^{-ct} \tag{7}$$

In the quasi-static pressure calculation equation (7), *c* is the leakage coefficient, representing the coefficient for the discharge of detonation products from the cabin. The value of *c* is calculated using equation (8). The value of *t* is the duration of quasi-static pressure.

$$c = 725\frac{\alpha_e A_s}{V} \tag{8}$$

Baker defined the value of α_e as the division of the area of the ventilation opening (A_v) by the area of the bulkhead (A_w). The surface area inside the cabin is represented by (A_s), and *V* represents the volume of the compartment.

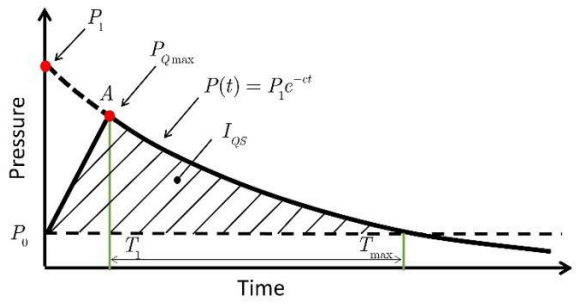


Figure 9 Baker's simplified quasi static pressure model.

In Figure 9 Baker proposed P_1 as equation (9):

$$P_1 = P_{Q\max} + P_0 \tag{9}$$

The quasi-static pressure results from the highpressure cabin environment created by multiple shock wave reflections. Unlike shock waves, the pressure throughout the entire cabin is nearly uniform. In the US military design manual TM5-1300 (1990), an empirical equation (10) is provided based on extensive experimental data analysis of damage effects.

$$P_{Q\max} = 2.25\left(W / V\right)^{0.72} \tag{10}$$

In equation (10), *W* denotes the masses of TNT, while *V* signifies the volume of the compartment.

The relative quasi-static pressure $\overline{P_1}$ calculated as equation (11):

$$\overline{P_1} = \frac{P_{Q\max} + P_0}{P_0} \tag{11}$$

The relative leakage coefficient $\bar{\tau}_{\max}$ calculated as equation (12):

$$\bar{\tau}_{\max} = 0.465 \ln \bar{P}_1 \tag{12}$$

The maximum quasi-static pressure time T_{max} calculated as equation (13):

$$T_{\max} = \bar{\tau}_{\max} \left(\frac{V}{\alpha_e A_s a_0} \right) \tag{13}$$

In equation (13), a_0 represents the speed of sound in air, assumed to be 340 m/s.

Baker introduced the impulse of quasi-static pressure, I_{QS} as shown in equation (14):

$$I_{QS} = \int_0^{T_{\max}} (P_{Q\max} e^{-ct} - P_0) dt \tag{14}$$

Baker's method for calculating quasi-static impulse appears to overestimate the value. Nevertheless, the quasi-static impulse value I_{QS}, when computed using equation (15) may be closer to the actual quasi-static impulse.

$$I_{QS} = \frac{T_1}{2} \left(P_{Q\max} - P_0 \right) + \int_{T_1}^{T_{\max}} (P_{Q\max} e^{-ct} - P_0) dt \tag{15}$$

The total impulse received at any point on the bulkhead I_T as shown in equation (16):

$$I_T = I_S + I_{QS} \tag{16}$$

Given the short duration of the explosion, it is assumed that a specific point on the wall instantly gains velocity. Upon this, Jones (1976) proposed initial impulse per response velocity V_0 at a particular point on the cabin wall, as shown in equation (17):

$$V_0 = \frac{I_T}{\rho t_e} \tag{17}$$

In equation (17), t_e is the equivalent thickness of wall, ρ represents the density of bulkheads.

2.2 Simplification of load in adjacent chamber

Li (2021) carried out an explosion test on neighboring compartments, with Figure 10 depicting a schematic diagram of the experiment. In Figure 10, TNT is placed in the explosion compartment volume denoted as V_c, and the pressure in the adjacent compartment is measured. A damaged plate separates the explosion chamber from the neighboring chambers. Through the test, Li observed the quasi-static pressure characteristics in the adjacent compartments, as shown in Figure 11, the pressure rises almost linearly from zero to its peak quasi-static value before gradually decreasing.

If the wall of the explosion compartment is damaged, the explosion compartment and adjacent compartments are treated as a single compartment, with the adjacent compartments' volume denoted as V_N. Following the explosion, a new compartment volume, V_{C+N} is established, which is the sum of V_c and V_N. The peak quasi-static pressure in the adjacent compartments is calculated using equation (10), assuming the TNT mass remains constant, and the peak pressure is related to the cabin volume.

Li analyzed the pressure-time domain curves for various prefabricated damage sizes and discovered that as the damage area increased, the rise time of quasi-static pressure decreased, yet the peak quasi-static pressure remained relatively unchanged. Consequently, leveraging this characteristic, P_{QmaxN} for quasi-static pressure in adjacent compartments was introduced as equation (18):

$$P_{QmaxN} = 2.26\left(\frac{m}{V_{C+N}}\right)^{0.72} \tag{18}$$

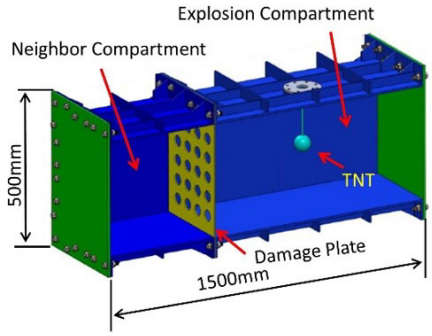


Figure 10 Quasi-static pressure test with partition damage.

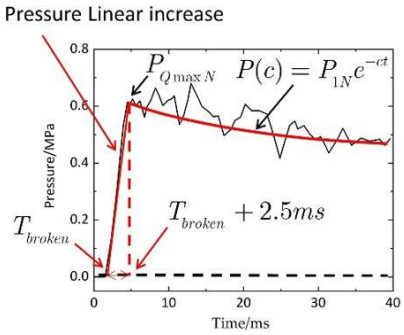


Figure 11 Simplification of adjacent compartment pressure.

During the period when the quasi-static pressure in adjacent compartments rises linearly, Li's experiment showed that with an opening area constituting 20% of the bulkhead area, the quasi-static pressure rise takes 2.5 ms. When the bulkhead entirely fails, the damaged area represents a larger portion of the bulkhead area. Therefore, it is assumed that the quasi-static pressure in adjacent compartments increases over 1 ms. The impulse of adjacent compartments calculated by equation (19):

$$I_{QSN} = \frac{P_{Q\max N}}{2} \cdot 0.001 + \int_{T_{broken}+0.001}^{T_{\max}} (P_{Q\max N}e^{-ct} - P_0)dt \tag{19}$$

In equation (19), T_{broken} is defined as the moment when the difference between the element velocity in the compartment containing TNT and the critical velocity is less than the margin of error. The velocity V_{0N} resulting from the impulse of quasi-static pressure is defined by equation (20):

$$V_{0N} = \frac{I_{QSN}}{\rho t_e} \tag{20}$$

2.3 Equivalent thickness of stiffened plate

When calculating the response of cabin wall to an explosion, it is important to consider the effect of stiffeners on the plate. Zhao et al. (2020) introduced the concept of equivalent thickness t_e for stiffened plates. The effectiveness of the equivalent thickness of the stiffened plate was verified through both experimental and simulation methods. Nan assumed the equity of the plate has equal masses with the stiffened plate, the stiffeners spread out the masses over the base plate. The equivalent thickness t_e can be calculated by:

$$t_e = t_p + \frac{V}{L^2} \tag{21}$$

where V is the total volume of stiffener, t_p and L are the thickness and width of the base plate, respectively.

2.4 Equivalent thickness of stiffened plate

An important experimental contribution to the field of structural plastic dynamic failure is the systematic study by Menkes and Opat (1973) on the mechanical behavior of fixed beams under uniformly distributed impact loads. They were the first to classify different failure modes, observing that as the impulse increased, various failure modes emerged. Building on these experimental findings, Jones (1976) performed a theoretical analysis of fixed-supported beams, providing the critical speed at which each failure mode occurs, as shown in equation (22):

$$V_{cr} = \frac{2\sqrt{2}}{3}\sqrt{\frac{\sigma_y}{\rho}} \tag{22}$$

In the equation (22): V_{cr} is the critical speed, m/s. σ_Y is the yield stress of the panel structure material, Pa. ρ is the density of the steel plate, kg/m^3.

According to Jones's experiment, assume that if the response speed V_0 at the calculation point exceeds the critical speed V_{cr} for bulkhead failure, the calculation point is considered to have failed. When the response speed V_0 at the calculation point is less than the critical speed V_{cr} for partition failure, deformation occurs at that calculation point. When V_0 =0, the structure is considered intact, as shown in equation (23).

$$\begin{cases} V_0 = 0 & \text{Intact} \\ 0 < V_0 < V_{cr} & \text{Deformed} \\ V_{cr} < V_0 & \text{Broken} \end{cases} \tag{23}$$

Figure 12 is a schematic diagram of the damage range under typical cabin explosion conditions.

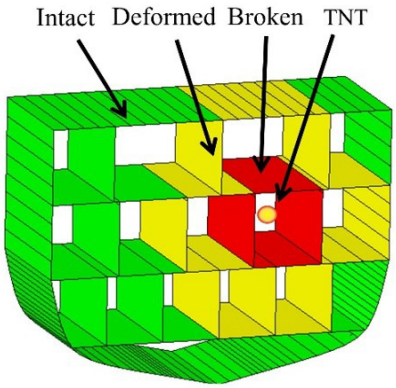


Figure 12 Schematic diagram of explosion damage range.

2.5 Verifying the range of damage resulting from an explosion inside the cabin

In order to investigate the range of damage caused by explosions inside the cabin, Yu et al. (2010) conducted tests on the explosion damage range. Figure 13 illustrates the overall diagram of the cabin explosion test, while Figure 14 depicts the typical failure mode of explosion damage inside the cabin. Yu's experimental data were utilized to validate the rationality of the theoretical calculation of explosion damage range.



Figure 13 Explosion test on ships with multiple compartments.

In the study by Yu, the damage characteristics of ship explosion tests were investigated. The test involved a steel plate with a thickness of t=3 mm, a charge of 0.05 kg, and a single compartment size of 0.15 x 0.125 x 0.1m. While specific compartment materials and yield strength were not provided by Yu, a tensile ultimate strength of 552MPa was given. Wei (2021) mentioned a ratio of common steel yield strength to tensile ultimate strength ranging from 0.8 to 0.95. Using this information, the relatively dangerous situation was analyzed, and the material yield strength was assumed to be σ_Y=552x 0.8=441.6MPa. In the case of a spherical TNT, the equivalent volume was calculated to be 3.048 x 10^{-5}m^3, assuming a TNT density of 1640kg/m^3, and the calculated TNT radius was 0.0213m.

The compartment containing the TNT is farthest in the length direction. Therefore, if this point is damaged, the panels in the width and height directions will also be damaged. Consequently, the measurement point is selected in the length direction for calculation. The proportional distance calculation results in Z=0.204, and the peak pressure in the length direction is calculated using equation (1) as ΔP=6.912MPa. Calculating the peak pressure of the reflected shock wave according to equation (4) gives P_R=51.437MPa. Equation (5) is used to calculate the duration of the shock wave as T_R=7.637×10^{-5}s. Following equation (6), the shock wave impulse I_s is calculated as 3437.232Pa·s and converted into a velocity of V_s=146.89m/s. Equation (22) is used to calculate the critical velocity as V_{cr}=224.298m/s. Upon comparing V_s and V_{cr}, it is determined that the current shock wave velocity V_s is less than V_{cr}. As a result, the shock wave did not damage the cabin walls, so the calculation continues with the quasi-static pressure phase.

During the quasi-static pressure stage, the peak quasi-static pressure P_1=24.033MPa is calculated using equations (9). Generally, when the explosives enter the interior of the cabin, the ventilation radius is typically larger than the diameter of the TNT. Assuming that the ventilation area is equivalent to the explosives, the calculated ventilation area A_v=0.00143m^2, the cabin wall area A_w is 0.0125m^2, and the cabin area A_s=0.092m^2, resulting in a calculated coefficient α_e=0.114. According to equation (8), the emission coefficient C=4089.113 is calculated. Following equations (11) and (12), the relative quasi-static pressure is found to be $\overline{P}_1$=238.86 MPa, and τ_{Max}=2.545. Using equation (13), the maximum duration time T_{max} for the quasi-static pressure is calculated to be 0.00133s. Based on equation (15), the quasi-static impulse I_{qs} is determined to be 41561.01Pa·s. According to equation (16), the total impulse I_T of the explosion compartment is calculated to be 44998.242Pa·s, and the equivalent velocity V_0=1776.112m/s. Comparing V_0 with V_{cr}, it is revealed that V_0 is greater than V_{cr}, indicating damage to the explosion compartment. The duration of the quasi-static pressure is then equally divided, assuming T_{broken}=8 × 10^{-5}s. This yields a total impulse I_{Total}=4063.232Pa·s and an elemental velocity of 173.642m/s. As the calculated elemental velocity is less than the critical velocity, the T_{broken} time is increased. Assuming T_{broken} =9×10^{-5}s, the total impulse I_{Total}=5475.232Pa·s, and the elemental velocity is found to be V_0=245.523m/s. Since the current elemental velocity exceeds the critical velocity, the value of T_{broken} is further adjusted. The average of the two T_{broken} values is calculated by assuming T_{broken} =8.5 × 10^{-5}s.

The explosion damaged the compartment, creating a large compartment consisting of six adjacent compartments, with the volume of the large compartment being the sum of the volumes of the seven small compartments. According to equation (18), P_{QmaxN} equals 5.92 MPa, while the ventilation area A_v and A_w remained unchanged, and A_s represented the combined area of the seven compartments. The value of A_w was 0.0125 m^2, with an emission coefficient of C = 2320.848. The relative quasi-static pressure $\overline{P}_1$ was 15.393 MPa, and the relative leakage coefficient τ_{Max} = 1.271. The maximum quasi-static pressure duration time was T_{max}=0.00116s. The calculation of the quasi-static impulse I_{QSN} resulted in 4518.01Pa·s, and the equivalent velocity V_0 was calculated to be 193.07 m/s. Since V_0 is less than the critical velocity but greater than 0, the cabin is considered to have undergone deformation. Given the current material properties are chosen for more precarious scenarios, adjacent compartments are not damaged in this situation, and generally will remain undamaged.

Table 1 presents the damage assessment of the cabin where the explosion occurred, providing calculated damage results for the compartment where the explosion took place. Table 2 presents the calculated damage for the adjacent compartments.

Table 1 Explosion compartment damage result.

t_e/mm	W/kg	σ_Y/Pa	Z	ΔP/Pa	P_R/Pa	T_r/s	I_s/Pa·s
3	0.05	441.6×10^6	0.204	6.912×10^6	51.437×10^6	7.637×10^{-5}	3437.32
V_s/(m/s)	V_{cr}/(m/s)	P_1/MPa	A_v/m^2	A_w/m^2	A_s/m^2	α_e	C
146.89	224.298	24.033	0.00143	0.0125	0.0925	0.114	4089.113
$\bar{P}_1$/MPa	τ_{max}	T_{max}/s	I_{qs}/Pa·s	I_T/Pa·s	V_{0T}/(m/s)	T_{broken}/s	
238.116	2.545	0.00133	41561.01	44998.242	1776.112	8.5×10^{-5}	

Table 2 Adjacent compartment damage results.

P_{QmaxN}/Pa	A_v/m^2	A_w/m^2	A_s/m^2	C	$\bar{P}_1$/MPa	τ_{max}	T_{max}/s	I_{QSN}/Pa·s	V_{0T}/(m/s)
5.92×10^6	0.00143	0.0125	0.368	2320.848	15.393	1.271	0.00116	4518.01	193.07

When comparing the explosion test depicted in Figure 14 with the theoretical calculation shown in Figure 15, it is apparent that the theoretical and experimental damage are analogous. The compartment where the explosion located incurs damage, while adjacent compartments become deformed. The theoretical calculation of the damage range demonstrates a degree of accuracy.

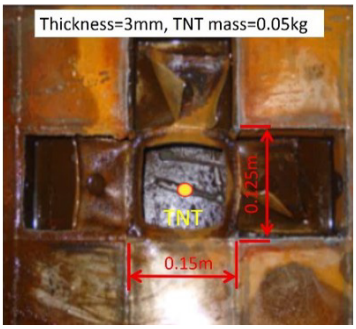


Figure 14 Damage range of explosion test inside the cabin.

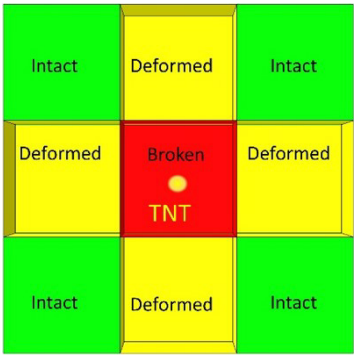


Figure 15 Theoretical calculation of damage range in cabin explosion.

2.6 Simplification strain-stress relationship of Smith element for deformation

Under explosive conditions, according to Menkes and Opat (1973), it was observed that structural dynamic failure primarily comprises deformation and damage. In the past, there has been limited research on the compressive bearing capacity of deformation plates during compression. Following the concept of plate structure buckling, the bearing capacity decreases significantly once the plate reaches the buckling deformation limit. To account for more adverse scenarios, it is assumed that the compressive strength of the deformed plate becomes 0.

The common methods for evaluating the strain-stress of plate elements, for example, Li used simulation (2019) and Xiong et.al (2022) used machine learning model prediction. The strain-stress relationship of plate elements after an explosion is more complex, Liu et.al (2013) utilized an indenter to simulate the deformation of the ship structure under external forces, providing crucial references for studying the tensile performance of deformed plate elements. Li et. al (2015) investigated the impact of deformation caused by indenters of various sizes, as depicted in Figure 16, on the tensile strength of the plate. The research suggests that different sizes of indenters in Figure 17 have a minimal effect on the plate's tensile strength. The maximum difference in tensile strength between different indenter groups and complete plates is only 3.2%.

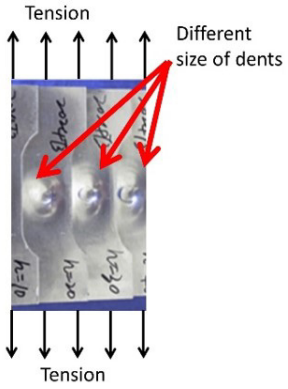


Figure 16 Tensile loading of plates with varying indentation sizes.

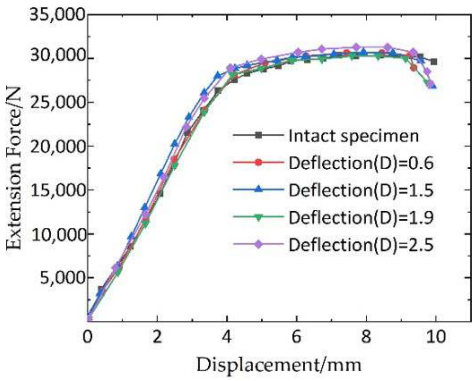


Figure 17 Tensile load and displacement curves of plates with varying indentation sizes.

Therefore, through analyzing the mechanical properties of deformed plates, a strain-stress equation (24) is proposed for deformed plates. In Figure 18, based on the concept of plate buckling, the load-bearing capacity of the plate decreases rapidly. Thus, it is assumed that the deformed plate is unable to withstand pressure, meaning that when compressed, the stress on the deformed plate is 0. When the deformed plate is under tension in the elastic stage, the stress due to deformation is equal to the elastic modulus multiplied by the strain. Once the strain value ε reaches the yield strain ε_s, the tensile stress $\sigma_{Deformation}$. of the deformed plate is equal to the yield stress σ_s.

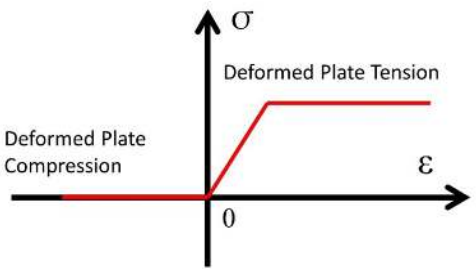


Figure 18 Characteristics of stress and strain in a deformed element.

$$\sigma_{Deformation} = \begin{cases} 0 & \varepsilon < 0 \\ E\varepsilon & 0 < \varepsilon < \varepsilon_s \\ \sigma_s & \varepsilon_s \leq \varepsilon \end{cases} \tag{24}$$

2.7 Explosion Smith method

For the convenience of research, the explosion Smith method proposes the following assumptions for ship hull breaches:(1) After the explosion, the ship can fully participate in the total longitudinal residual strength bearing capacity. (2) Discrete into regular geometric shapes. (3) In the calculation of load increment, the shape, position, and size of the break remain unchanged.

Figure 19 shows the flowchart of the explosion Smith method. Firstly, a geometric matrix *G* is established based on the analysis model, and the element numbers are initialized, i.e. *i*=0. The incident shock wave and reflected shock wave parameters are calculated based on the location and masses of the TNT, and the time-domain curves of each element's shock wave are obtained. The impulse value of each element's shock wave is calculated and converted into the velocity of each element. Next, the critical speed is calculated and the element speed is compared with the critical speed value. If the element speed is greater than the critical speed, the geometric matrix value of the element is set to 0. If the critical speed of the element is less than the critical speed, it will proceed to the next element calculation.

After calculating the range of shock wave damage for all elements, the next step is to calculate the quasi-static pressure curve, integrate it to obtain the impulse, and then convert it into velocity. Following this, the shock wave velocity and quasi-static velocity for each element are added together. If the calculated velocity value is greater than the critical velocity, the geometric matrix value of that element is set to 0. If the velocity of the element is less than the critical velocity, the calculation proceeds to the next element.

After completing the shock wave and quasi-static pressure stages, the next step is to calculate the residual strength of each element. This involves initializing the curvature of the element and gradually increasing the curvature value. The strain of the element is then calculated based on the curvature, and the stress value is determined using the strain-stress relationship of the element. Following this, the force on each element is calculated according to the stress definition, and the bending moment on the neutral axis is determined. The position of the neutral axis is calculated according to the force balance criterion, and then a verification is conducted to check if the resultant force, neutral axis position, curvature increment, element number, etc., exceed the critical value. If not, the calculation proceeds to the next element. If they exceed the critical value, the curvature bending moment curve is outputted to calculate the residual strength of the ship under explosion conditions.

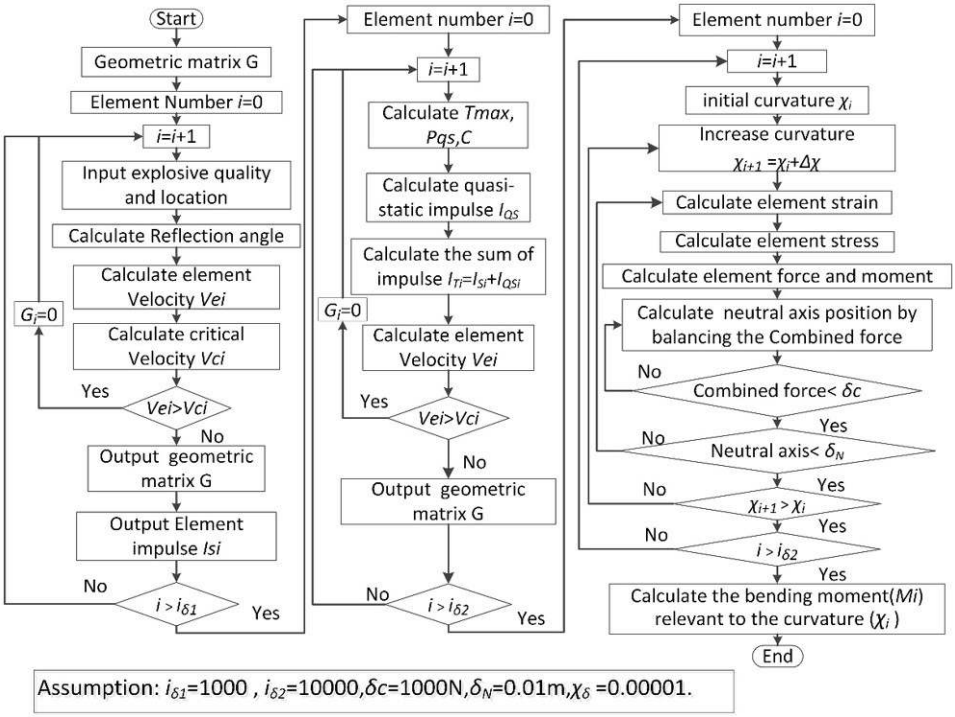


Figure 19 Explosion Smith method flowchart.

3 Numerical Simulation model

Simulations were carried out to confirm the feasibility of the explosion Smith method and revealed the residual strength characteristics of the ship under explosion conditions.

3.1 Explosion and Residual Strength Simulation settings

In order to account for the movement of explosive products within the cabin, the ALE method in LS-DYNA was utilized for the simulation. The model's dimensions and TNT placement are illustrated in Figure 20. The air domain measures 5m x 5m x 12m, while the ship's dimensions are 3.66m x 2.8m x 9m. Additionally, taking into consideration the stiffened plate, the hull's equivalent thickness is 5mm. The current ship model comprises three compartments in the z direction, each with a length of 3m. To analyze the impact of TNT at various positions and masses on the residual strength of ships, a middle section was chosen at the model's midpoint along the z-direction, and a total of 16 simulation setups were established involving 4 different positions and 4 different masses of TNT. The TNT is positioned at the center of each respective compartment.

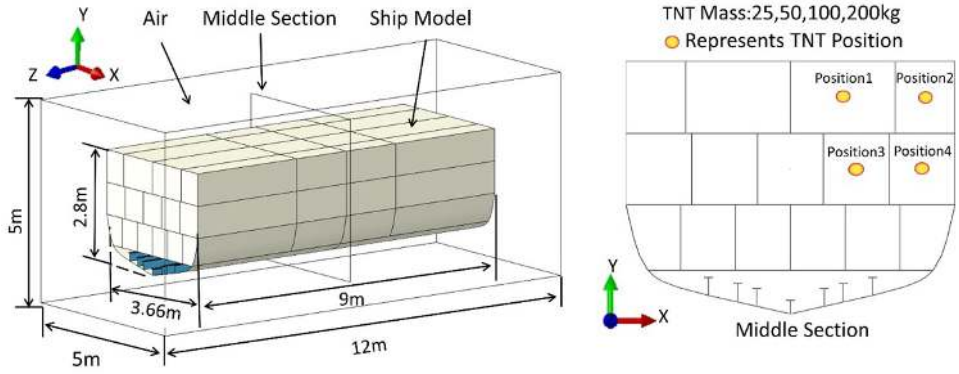


Figure 20 The location of the ship and TNT.

Table 3 presents the working conditions for various positions and TNT masses. In Table 3, numbers 1 to 4 represent the TNT located at position 1 with quantities of 25kg, 50kg, 100kg, and 200kg respectively. Similarly, numbers 5 to 8 correspond to the TNT at position 2 with quantities of 25kg, 50kg, 100kg, and 200kg respectively. In the same way, numbers 9 to 16 also represent different quantities of TNT at positions 3 and 4, respectively.

Table 3 Working condition table.

No.	Position	TNT Masses/kg	No.	Position	TNT Masses/kg
1	1	25	9	3	25
2	1	50	10	3	50
3	1	100	11	3	100
4	1	200	12	3	200
5	2	25	13	4	25
6	2	50	14	4	50
7	2	100	15	4	100
8	2	200	16	4	200

Figure 21 displays the schematic diagram of longitudinal loading. One side of the model is simply supported, while the other side has a displacement boundary. All nodes on the side face are coupled at the center point of the end face, with constraints on the movement degrees of freedom in the x and y directions, as well as the rotational degrees of freedom in the y and z directions. The nodes in the section are rotated by 0.2° around the x axis for the calculation of residual strength under explosive conditions.

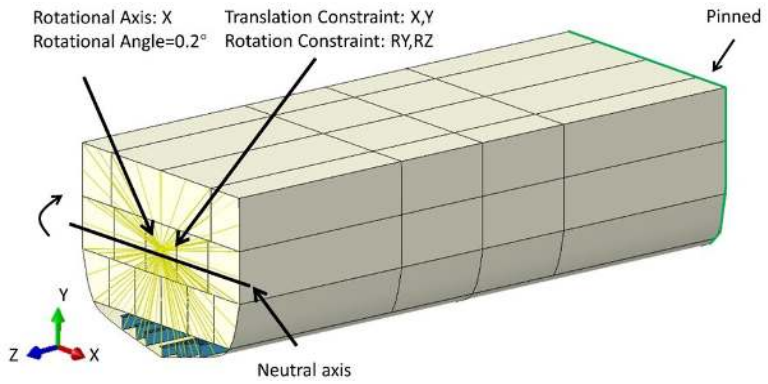


Figure 21 Schematic diagram of longitudinal loading.

3.2 Equation of state and constitutive model

The JWL equation of state is frequently used in simulations to describe the pressure generated by detonation products. The specific equation is illustrated in equation (25), while the parameters of the JWL equation for TNT explosive can be found in Table 4. The TNT material parameter and JWL equation reference from Gao (2014).

$$p = A\left(1-\frac{\omega}{R_1 v}\right)e^{-R_1 v} + B\left(1-\frac{\omega}{R_2 v}\right)e^{-R_2 v} + \frac{\omega e}{v} \tag{25}$$

where p is the pressure A, B, R_1, R_2, ω are constants, v is relative volume and e is specific internal energy.

The ideal gas equation of state is utilized to describe the air, with the linear polynomial state equation for air presented in Table 5. The air material parameter also references from Gao (2014).

Q345B steel is chosen as the ship material. The Cowper-Symonds model is employed as the constitutive model, considering the strain rate strengthening effect of the material. The specific expression is provided in equation (26), and the main parameters of the C-S model are listed in Table 6. The Q345 material parameter reference from Gao (2023).

$$\frac{\sigma_d}{\sigma_s} = 1 + \left(\frac{\dot{\varepsilon}}{C}\right)^{1/p} \tag{26}$$

Where σ_d is dynamic yield stress, σ_s is static yield stress, $\dot{\varepsilon}$ is equivalent strain rate, C, P are Strain rate parameters. The failure strain is 0.28.

Table 4. Material parameters of TNT.

ρ/(kg/m³)	D_{CJ}/(m/s)	P_{CJ}/GPa	E_0/GPa	A/GPa	B/GPa	R_1	R_2	ω
1610	6930	21	7.0	371.2	3.231	4.15	0.95	0.30

Table 5. Material parameters of Air.

ρ/(kg/m³)	C_0/Pa	C_1/Pa	C_2/Pa	C_3/Pa	C_4/Pa	C_5/Pa	C_6/Pa	E_0/Pa	V_0
1.29	0	0	0	0	0.401	0.401	0	2.5×10^5	1.0

Table 6. Material parameters of Q345B.

ρ/(kg/m³)	E/GPa	υ	σ_s/MPa	C	P	ε_f
7850	210	0.3	345	4000	5	0.28

4 Mesh Sensitivity Analysis

Both LS-DYNA simulation and the explosion Smith method discretize the structure. To clarify terminology: in LS-DYNA simulation, it's referred to as mesh, whereas in the explosion Smith method, it's termed element. In mesh sensitive analysis, the object of analysis is the impact of mesh on LS-DYNA simulation.

The mesh utilized in a simulation significantly affects the analysis results. Generally, as the number of meshes increases, the simulation results gradually converge, but the computational workload also increases. Therefore, it is crucial to accurately determine the number of meshes to balance convergence and calculation accuracy.

To examine the mesh sensitivity of the residual strength of the ship, mesh sizes of 0.3 m, 0.2 m, 0.02 m, 0.1 m, and 0.025 m were utilized, with corresponding total mesh numbers of 7,348, 10,565, 30,421, 72,152, and 192,037 respectively. As illustrated in Figure 22, the residual strength of the ship with different mesh sizes was calculated, and it was found that the residual strength decreased as the number of meshes increased. The residual strengths for different meshes were 3.442×10^7 N·m, 3.123×10^7 N·m, 2.955×10^7 N·m, and 2.885×10^7 N·m, 2.863×10^7 N·m respectively. Given the impact of air mesh size on the residual strength of ships under explosion conditions, the ship mesh size is set to 0.1m, and the air mesh sizes are set to 0.3m, 0.2m, 0.1m, 0.05m, and 0.025m, respectively. The corresponding number of meshes are 19,200, 37,500, 87,120, 300,000, and 718,240, respectively. As illustrated in Figure 22, the residual strength of the ship was calculated under different air mesh sizes and TNT masses conditions at position 1. It was observed that the residual strength decreased as the number of meshes increased.

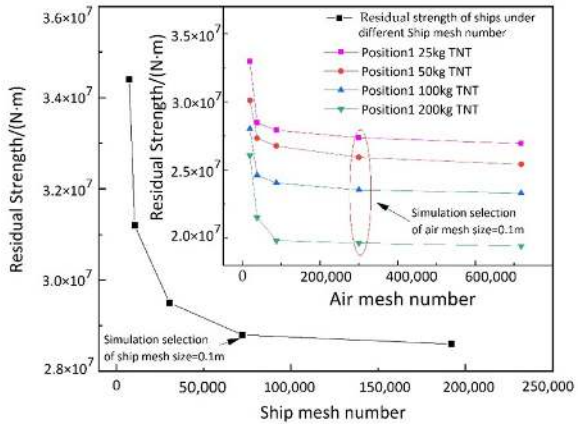


Figure 22 Mesh sensitivity analysis of ship residual strength.

Taking position 1 as an example, the TNT with a mass of 25kg, the residual strength of different meshes were 3.296×10^7 N · m, 2.845×10^7 N · m, 2.791×10^7 N · m, 2.736×10^7 N · m, and 2.694×10^7 N · m, respectively. The TNT with a mass of 50kg has residual strengths of 3.012×10^7 N · m, 2.733×10^7 N · m, 2.676×10^7 N · m, and 2.593×10^7 N · m, 2.541×10^7 N · m for different meshes, respectively. The TNT with a mass of 100kg has residual strengths of 2.802×10^7 N · m, 2.461×10^7 N · m, 2.405×10^7 N · m, and 2.353×10^7 N · m and 2.33×10^7 N · m for different meshes, respectively. The TNT with mass of 200kg has residual strengths of 2.606×10^7 N · m, 2.151×10^7 N · m, 1.981×10^7 N · m, and 1.964×10^7 N · m, 1.941×10^7 N · m for different meshes, respectively.

To ensure the accuracy of the calculation results while considering the calculation speed, the ship's mesh configuration is shown in Figure 23, which includes both an overall view and an enlarged section. The overall mesh size of the ship was 0.1 m, with a quadrilateral mesh type and a total of 72,152 meshes. For the air domain, the mesh size is 0.1 m, the mesh type is hexahedral, and the total number of mesh is 300,000.

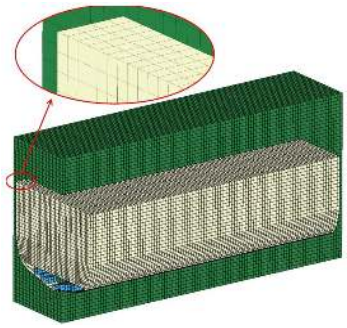


Figure 23 Overall and enlarged view of ship and air mesh.

5 Strain Rate Sensitivity Analysis

Strain rate is crucial for explosion calculations. Harding (1983) found that explosion strain rates generally range between 10 and 1000. Azevedo and Alves (2008) analyzed the influencing parameters of strain rate, providing an important reference for strain sensitivity analysis. On the other hand, the effect of strain rate on yield stress impacts the extent of explosion damage and, consequently, the residual strength of the ship. In simulation calculations using the Cowper-Symonds model, the parameters that affect strain rate are C and P. Yu et al. (2010), Meng et al. (2019), and Jiang et al. (2020) measured the stress-strain relationship of Q345B under various strain rate conditions. To perform a strain rate sensitivity analysis, different Cowper-Symonds strain rate influence parameters, *C* and *P*, were used to assess their impact on the ship's residual strength in Figure 24 and Figure 25.

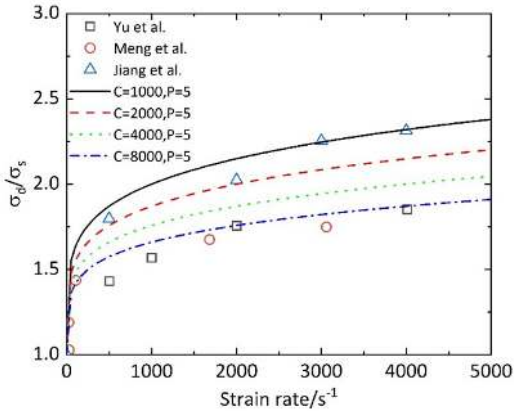


Figure 24 The influence of different strain rate coefficients C.

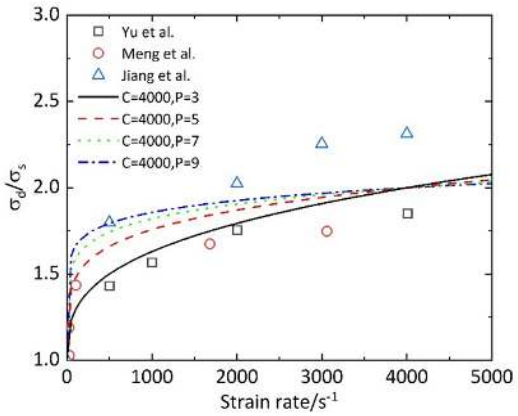


Figure 25 The influence of different strain rate coefficients P.

From Figure 24, it can be observed that the strain rate influence coefficient *C* is inversely proportional to σ_d/σ_s, meaning that the larger the value of *C*, the greater the dynamic stress value σ_d, resulting in less deformation of the hull and thus less reduction in its ultimate strength. From Figure 25, it can be observed that the strain rate influence coefficient *P* is directly proportional to the dynamic stress value σ_d when the strain rate is less than 4000. That is, the larger the value of *P*, the greater the dynamic stress σ_d. However, when the strain rate is greater than 4000, the strain rate influence coefficient *P* is inversely proportional to the dynamic stress value σ_d. If the range of cabin damage is consistent, the greater the dynamic stress σ_d, the less the reduction in the ultimate strength of the hull. Similarly, if the range of cabin damage is the same, the smaller the dynamic stress σ_d, the more the ultimate strength of the ship decreases. However, the relationship between actual ship strain rate and residual strength may be more complex, and further research can be conducted in the future.

In this article, factors such as different material processes and potential measurement errors are considered. The selection of strain rate parameters is closer to the average values of experimental data from Yu et al. (2010), Meng et al. (2019), and Jiang et al. (2020), that is, *C*=4000 and *P*=5 are chosen as the Cowper-Symonds strain rate parameters for simulation.

6 RESULTS

6.1 Simulation and theoretical calculation of explosion damage range

Figure 26 illustrates the damage range caused by different TNT masses at position 1. Through simulation results, it can be observed that in Figure 26 (a) and (c), the cabin undergoes deformation after the explosion, with the maximum stress values being 398 MPa and 755 MPa, respectively. The theoretical calculation results in Figure 26 (b) and (d) are consistent with the simulation results, both indicating that the structure has undergone deformation. Figure 26 (e) shows the TNT masses of 100 kg, with a maximum stress of 685 MPa. In the simulation, the compartment where the TNT is located is damaged, and the explosive products diffuse to adjacent compartments. It can be observed that adjacent compartments have undergone deformation under quasi-static pressure. Figure 26 (g) shows the TNT masses of 200 kg, and the compartment where the TNT is located is damaged. The explosive products diffuse to adjacent compartments, and the rightmost compartment on the first and second decks is also damaged under quasi-static pressure. This is because this compartment has the smallest volume among adjacent compartments, so it is the first to be damaged, indicating that quasi-static pressure first damage smaller compartments. Comparing the damage range of Figure 26(e), (g)and Figure 26(f), (h), it can be found that the damage ranges of both are consistent. However, comparing the simulation and theoretical calculations at position 1, it can be found that the simulation can better reflect the degree of cabin deformation. Although theoretical calculations can determine the deformation of the cabin, they do not reflect the degree of cabin deformation, indicating certain limitations.

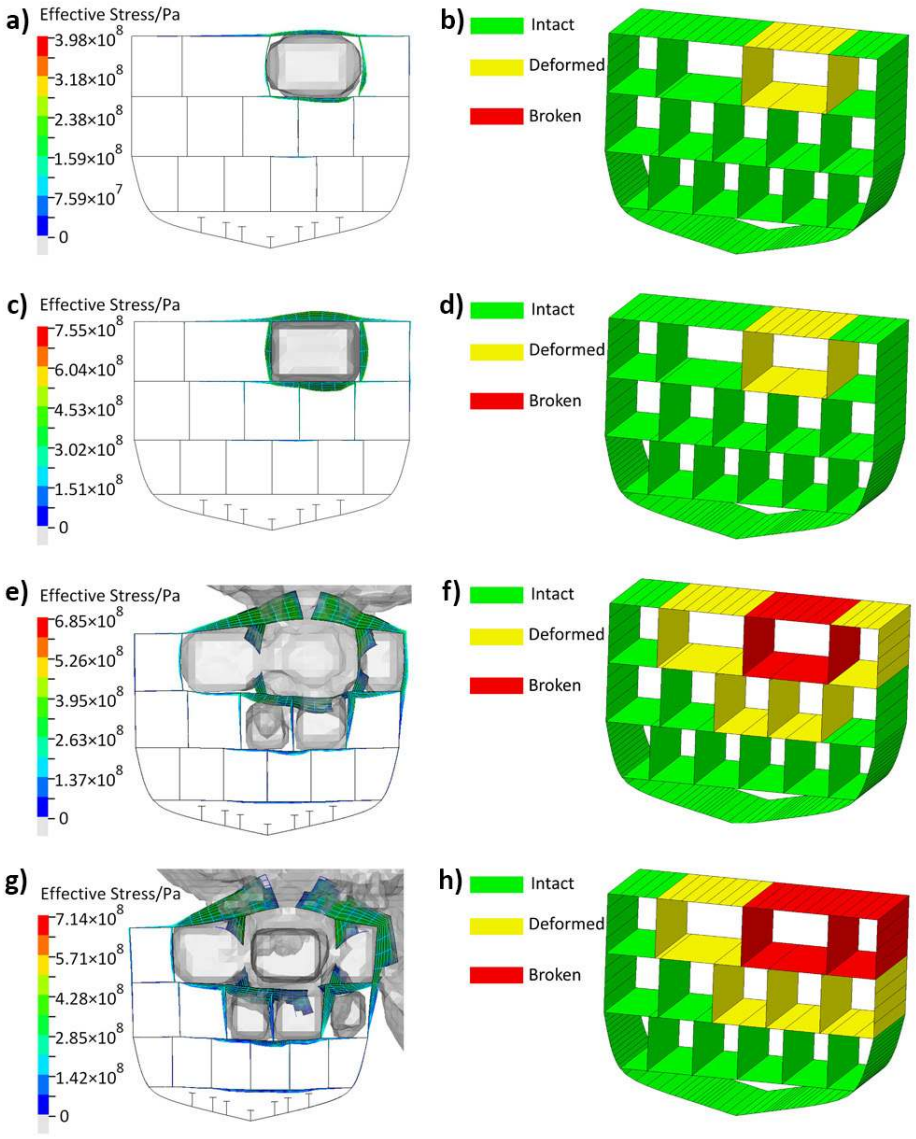


Figure 26 Simulation and theoretical calculation of explosion damage range at position 1

Figure 27 illustrates the damage range of different TNT masses at position 2. Through simulation, it can be observed that when the masses of the TNT in Figure 27 (a) is 25 kg, the cabin undergoes deformation but no damage occurs, with a maximum stress of 467 MPa. Figure 27 (b) shows that the theoretical calculation results are consistent with the simulation results, and the cabin undergoes deformation. In Figure 27 (c), the masses of the TNT are 50 kg, and the compartment where the explosion occurs is damaged. The explosion product diffuses from the rupture to the adjacent compartment, causing deformation, with a maximum stress of 647 MPa. Figure 27 (e) shows that the masses of the TNT are 100 kg, and the maximum stress is 684 MPa. The compartment where the TNT is located is damaged, and the deformation degree of adjacent compartments is greater than with 50 kg. From Figure 27 (e), it can be seen that due to the diffusion of explosion products from the rupture to the outside of the compartment, a good ventilation environment is formed, which weakens the quasi-static pressure damage effect. Figure 27 (g) shows that the masses of the TNT are 200 kg, and the compartment where the explosion occurs is damaged. The adjacent compartments have greater deformation compared to Figure 27 (c) and (e), but there is no damage to the adjacent compartments. In Figure 27 (d), (f), and (h), theoretical methods calculate that the compartment where TNT is located is damaged, and adjacent compartments are deformed. By comparing the results of simulation and theoretical methods, it was found that the range of explosion damage in the cabin calculated by simulation and theoretical methods is consistent.

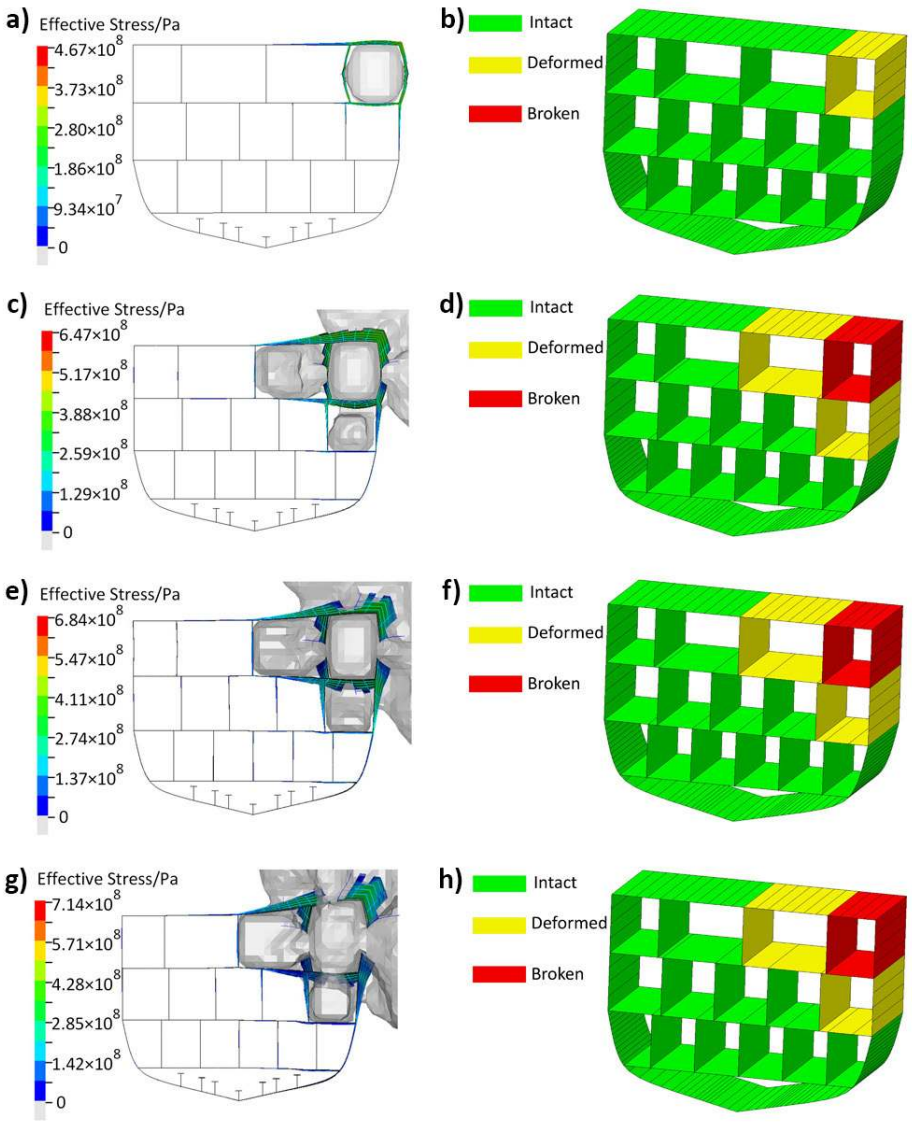


Figure 27 Simulation and theoretical calculation of explosion damage range at position 2

Figure 28 illustrates the damage range of different TNT masses at position 3. In Figure 28 (a), with TNT masses of 25 kg, the cabin undergoes deformation with a maximum stress of 577 MPa. Figure 28 (b) shows the theoretical method

for calculating cabin deformation. Figure 28 (c) shows that with TNT masses of 50 kg, the compartment where the TNT is located is damaged, and the explosion products diffuse to adjacent compartments. The adjacent compartments undergo deformation under quasi-static pressure, with a maximum stress of 579 MPa. In Figure 28 (e), with TNT masses of 100 kg, the compartment where the TNT is located is damaged, and the explosion products diffuse to adjacent compartments, with a maximum stress of 636 MPa. Figure 28 (g) shows that with TNT masses of 200 kg, the compartment where the TNT is located is damaged, and the explosion products diffuse to adjacent compartments, causing greater deformation than in Figures 28 (c) and 28 (e), with a maximum stress of 656 MPa. It can be observed that at position 3, due to the proximity of the TNT to the center of the compartment, the damage range is larger than at other positions, but it does not cause damage to the top deck. Comparing the simulation and theoretical calculation of the damage range at position 3, although there is a difference in the results between Figure 28 (c) and (d), as in Figure 28 (c), the longitudinal bulkheads of adjacent compartments at the bottom have increased structural strength, resulting in incomplete damage to the bulkheads. However, as the TNT masses increases, this phenomenon disappears, and the damage range of Figure 28(e), (g) and Figure 28(f), (h) is consistent.

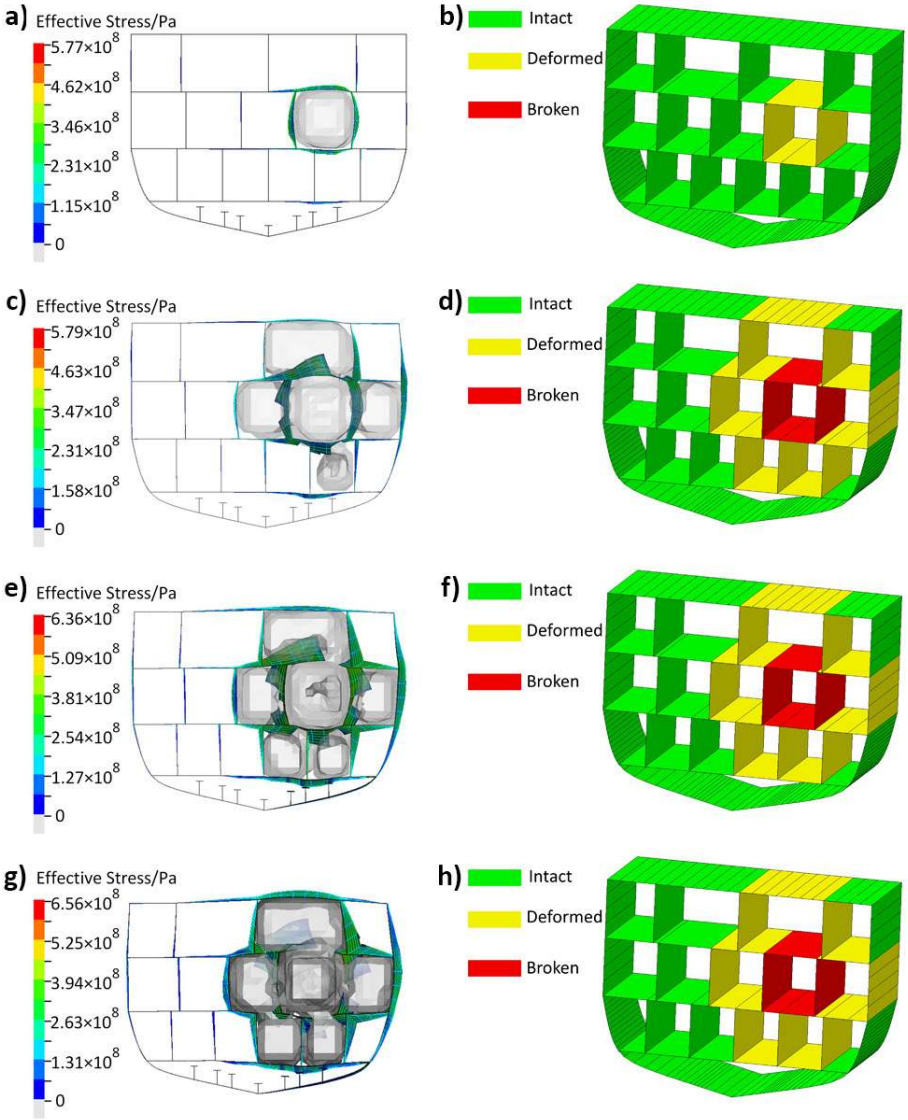


Figure 28 Simulation and theoretical calculation of explosion damage range at position 3

Figure 29 illustrates the damage range of different TNT masses at position 4. In Figure 29 (a), with TNT masses of 25 kg, the cabin undergoes deformation with a maximum stress of 504 MPa. Figure 29 (c) shows that with TNT masses of 50 kg, the explosion compartment is damaged and the explosion products diffuse. Adjacent compartments undergo deformation under quasi-static pressure, with a maximum stress of 619 MPa. In Figure 29 (e), with TNT masses of 100 kg, the compartment where the TNT is located is damaged, and the explosion products diffuse to adjacent chambers, with

a maximum stress of 693 MPa. In Figure 29 (g), with TNT masses of 200 kg, the compartment where the TNT is located is damaged, and the explosion products diffuse to adjacent chambers, causing greater deformation than in Figures 29 (c) and 29 (e). It can be observed that due to the proximity of position 4 to the ship's side, the explosion products form a good ventilation environment after damaging the compartment where the TNT is located, resulting in deformation of adjacent compartments with increased TNT masses, but without damage.

It can be observed that there are differences between the simulation and theoretical calculation in Figure 29 (c). The theoretical calculation results show a larger range of damage, and the analysis indicates that the support effect of the top bulkhead increases the local strength. However, as the TNT masses increases, the simulation calculation and theoretical calculation in Figures 29 (e), (g)and 29 (f), (h)show the same damage range.

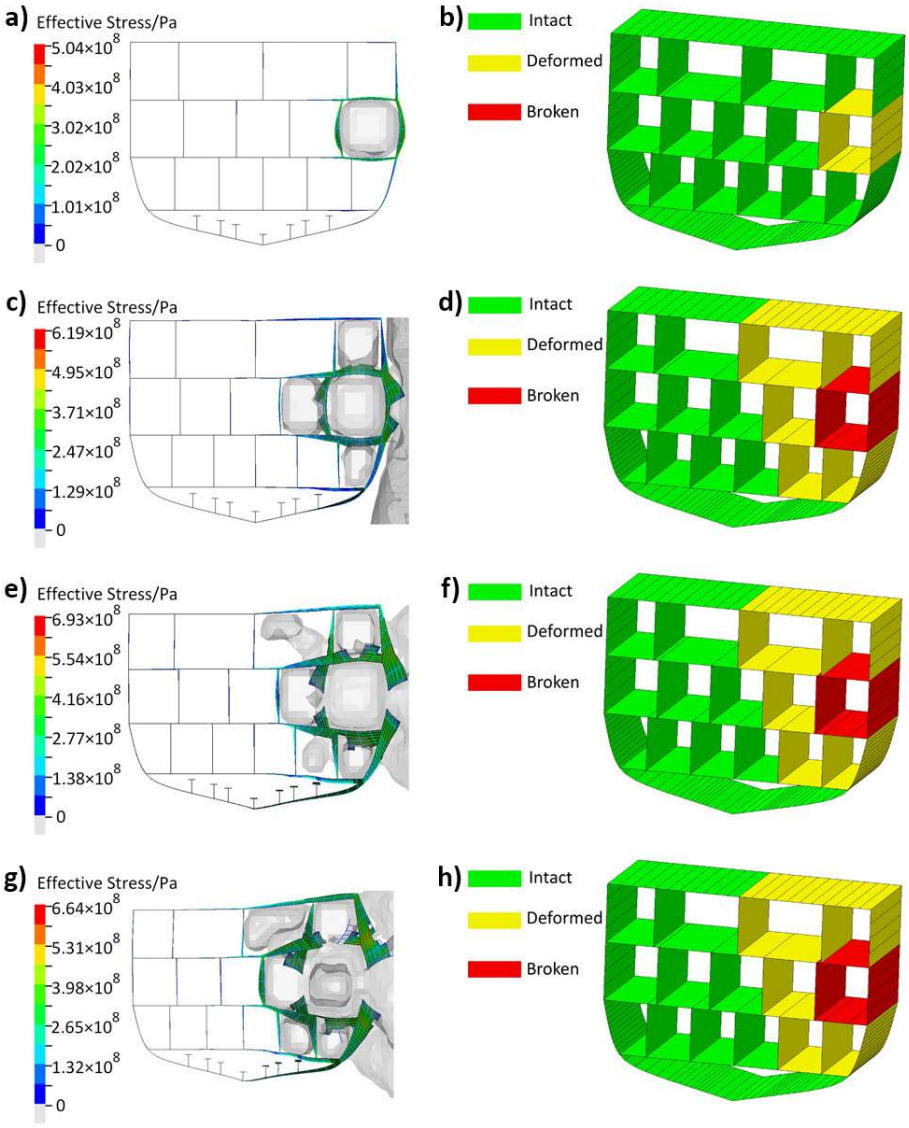


Figure 29 Simulation and theoretical calculation of explosion damage range at position 4

6.2 Residual strength of simulation and explosion Smith method

After the ship explosion, the residual strength was calculated using simulation and the explosion Smith method. As shown in Figure 30, it can be observed that with continuous loading as depicted in Figure 21, the residual strength of the ship increases rapidly from 0 and then slowly decreases after reaching its maximum value. During this process, the maximum value represents the residual strength. Comparing the residual strength results of the explosion Smith method and simulation, it was found that the trends of the two are consistent. For the same location, as the TNT mass increases, the residual strength decreases. This phenomenon indicates that as the mass of TNT increases, the damage to the hull also increases, leading to a decrease in the hull's ability to longitudinal bending.

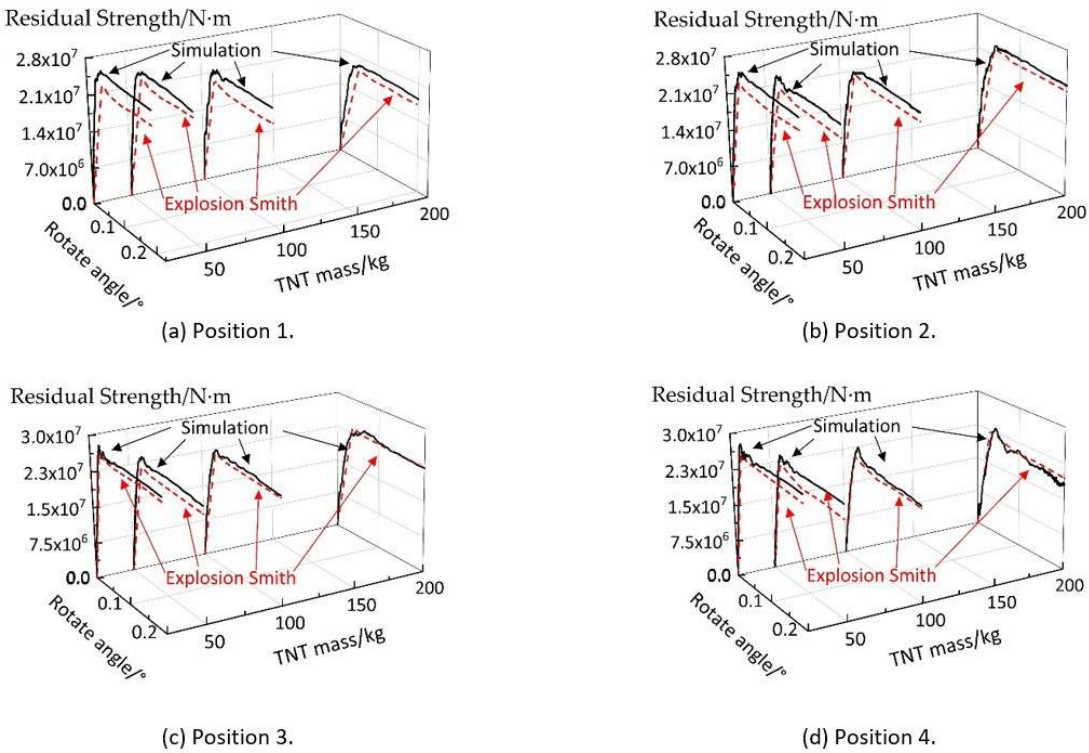


Figure 30 Comparison between simulation method and explosion Smith method for residual strength of ship hull after explosion

6.3 Residual strength characteristics of ship after explosion

To further analyze the residual strength characteristics under four different TNT masses and locations, extract the residual strength values for each working condition from Figure 30, as shown in Table 7 and Figure 31. By comparing the working conditions of TNT at different positions, it can be observed that when TNT is close to the top deck, such as in position 1 and position 2, the residual strength decreases more significantly. Due to the damage to the top decks of three compartments at position 1, the residual strength decreased the most. Both position 2 and position 4 caused damage to two top decks, resulting in similar outcomes. However, position 4 caused a larger range of damage, leading to a slightly smaller decrease in residual strength compared to position 2. While position 3 had a larger range of damage, it only caused deformation of one top deck, and the other damaged compartments were close to the neutral axis, resulting in minimal impact on the residual strength of the ship.

Comparing the results of the simulation and the explosion Smith method, the two trends are consistent. However, the results of the explosion Smith method are smaller compared to the simulation results. This is because the compression element performance assumed by the explosion Smith method is relatively strict. Although the bearing capacity of the plate structure significantly decreases after deformation, it can still continue to bear the load. As the masses of the TNT increases, the deformation of the cabin intensifies, and the discrepancies between the simulation calculations and the explosion Smith method results gradually decrease.

Table 7 Residual strength value and error of explosion Smith method and simulation.

No.	Position1			No.	Position2		
	Simulation	Explosion Smith	Error (%)		Simulation	Explosion Smith	Error (%)
1	2.736× 10^7	2.473× 10^7	9.6	5	2.702× 10^7	2.523× 10^7	6.6
2	2.593× 10^7	2.473× 10^7	4.6	6	2.468× 10^7	2.217× 10^7	10.2
3	2.353× 10^7	2.157× 10^7	8.3	7	2.359× 10^7	2.217× 10^7	6.0
4	1.964× 10^7	1.893× 10^7	3.6	8	2.309× 10^7	2.217× 10^7	4.0
No.	**Position3**			**No.**	**Position4**		
	Simulation	**Explosion Smith**	**Error (%)**		**Simulation**	**Explosion Smith**	**Error (%)**
9	2.918× 10^7	2.793× 10^7	4.3	13	2.916× 10^7	2.793× 10^7	4.3
10	2.592× 10^7	2.351× 10^7	9.3	14	2.552× 10^7	2.229× 10^7	12.6
11	2.456× 10^7	2.351× 10^7	4.3	15	2.359× 10^7	2.229× 10^7	5.5
12	2.412× 10^7	2.351× 10^7	2.5	16	2.297× 10^7	2.229× 10^7	3.0

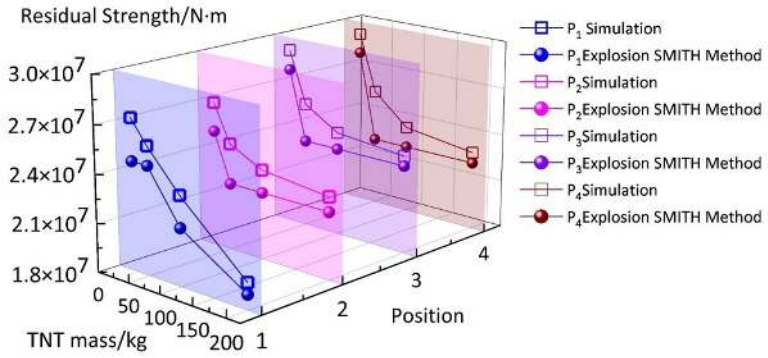


Figure 31 Comparison of the residual strength simulation and explosion Smith method for ships in different TNT masses and position

7 CONCLUSION

(1) Both the explosion Smith method and simulation can evaluate the impact of explosions on the residual strength of the ship, and the trend is consistent.

(2) By comparing different positions of TNT, it was found that the closer the TNT is to the interior of the top cabin, the larger the damage residual strength. When the TNT is placed in a relatively external cabin, the explosion products are discharged outside the cabin during the explosion, creating an open ventilation boundary and reducing the damage residual strength.

(3) When comparing the simulation and theoretical calculation of the ship explosion damage range, it can be seen that the results are mostly consistent. However, under some conditions with small TNT mass, the simulation shows a smaller damage range compared to the theoretical calculation. This can be attributed to the closer proximity between the longitudinal bulkheads of different layers, resulting in local strength enhancement. Nevertheless, this phenomenon diminishes as the mass of the TNT increases, and the simulation results eventually align with the theoretical calculation of the damage range.

(4) In contrast to simulations, the current theoretical calculations only depict the structural state after an explosion and cannot offer specific deformation values, leading to more stringent conditions in the deformation area during residual strength calculations. Nevertheless, as the mass of TNT increases, the ship's deformation becomes more pronounced, and the error gradually diminishes.

(5) When specifying the mechanical properties of deformed elements, it is assumed that the compress-bearing capacity after deformation is 0. However, in simulation, the deformed plate still bears a certain amount of load, leading to more pessimistic explosion Smith results compared to simulation. In the future, tests can be performed to assess the compressive strength of the deformed plate and improve the accuracy of the explosion Smith method.

Author's Contribuitions: Conceptualization, J.X Wu. and M. Yan; Methodology, J.X Wu; Investigation, J.X Wu; Writing - original draft, J.X Wu; Writing - review & editing, J.X Wu; Funding acquisition, M. Yan and X.W. Sun; Resources, M. Yan; Supervision, M. Yan and X.W. Sun.

Editor: Marcílio Alves

References

Anna C. (2024). Red Sea Crisis: How Global Trade Is Being Upended by Attacks on Container Ships | CNN Business Available online: https://edition.cnn.com/2024/02/08/business/red-sea-crisis-global-trade-explained/index.html.

Arora, H., Kelly, M., Worley, A., Del Linz, P., Fergusson, A., Hooper, P.A., Dear, J.P. (2014). Compressive Strength after Blast of Sandwich Composite Materials. Phil. Trans. R. Soc. A 372: 20130212, doi:10.1098/rsta.2013.0212.

Azevedo, Ricardo L., and M. Alves. (2008). A numerical investigation on the visco-plastic response of structures to different pulse loading shapes. Engineering Structures.30.1:258-267, doi: 10.1016/j.engstruct.2007.04.002.

Beshara, F.B.A. (1994). Modelling of Blast Loading on Aboveground Structures—II. Internal Blast and Ground Shock. Computers & Structures 51: 597–606, doi:10.1016/0045-7949(94)90067-1.

Bhardwaj, U., Teixeira, A.P., Guedes Soares, C., Ariffin, A.K. Singh, S.S. (2021). Evidence Based Risk Analysis of Fire and Explosion Accident Scenarios in FPSOs. Reliability Engineering & System Safety 215: 107904, doi: 10.1016/j.ress.2021.107904.

Calle, M. A. G., R. E. Oshiro, and M. Alves. (2017). Ship collision and grounding: Scaled experiments and numerical analysis. International journal of impact engineering 103: 195-210.

Cerik, B.C. (2018). Ultimate Longitudinal Compressive Strength of Steel Plates with Lateral Patch Load Induced Plastic Deformation. Thin-Walled Structures 122: 416–424, doi: 10.1016/j.tws.2017.10.030.

Qiao, C., Shi-lian, Z., Shao-bo, W., Yi-kan, Z. (2017). New Impulsive Factor in Representing Cabin Damage under External Air Explosion. Journal of Ship Mechanics 21: 761–768, doi: 10.3969/j.issn.1007-7294.2017.06.010.

EMSA Annual Overview of Marine Casualties and Incidents 2023. (2024). Available online: https://www.emsa.europa.eu/we-do/safety/accident-investigation/items.html?cid=141&id=5052.

Gao, F., Ji, C., Long, Y., Song, K. (2014). Dynamic responses and damages of water-filled cylindrical shell subjected to explosion impact laterally. Latin American Journal of Solids and Structures 11: 1924-1940.

Gao, H., Tian, H., Gao, X. (2023). Damage Characteristics of Cabin in Navigational State Subjected to Near-Field Underwater Explosion. Ocean Engineering 277 :114256, doi: 10.1016/j.oceaneng.2023.114256.

Go, G.-H., Cao, V.-H., Kim, Y., Choi, H.-J., Oh, S.-W., Kim, M.-J. (2023). Evaluation of the Dynamic Stability of Underground Structures Assuming a Hydrogen Gas Explosion Disaster in a Shallow Underground Hydrogen Storage Facility. Applied Sciences 13: 12317, doi:10.3390/app132212317.

Harding, J. (1983). High-Rate Straining and Mechanical Properties of Materials. Springer Netherlands, doi: 10.1007/978-94-011-9751-9_4.

Huang, X., Guo, J., Miao, Y., Xie, X., Li, Y., Wang, H., Huang, F. (2023). A Study on the Roof-Cutting and Pressure Releasing Technology of Roof Blasting. Applied Sciences 13: 9968, doi:10.3390/app13179968.

Jaidaa, T. Possible Red Sea Oil Spill After Houthi Attack. (2024). Available online: https://www.marinelink.com/news/possible-red-sea-oil-spill-houthi-attack-515234.

Jiang, Tao, et al. (2020). Experimental investigation on mechanical behaviors of Q345B steel material over wide ranges of strain rates and temperatures. Journal of the Brazilian Society of Mechanical Sciences and Engineering 42.10:537.

Jones, N. Plastic Failure of Ductile Beams Loaded Dynamically. (1976). Journal of Engineering for Industry 98: 131–136, doi:10.1115/1.3438805.

Khalifa, Y. (2015). BLAST DAMAGE MITIGATION IN SUBMERGED SYSTEMS. PHASE I: INTERNAL EXPLOSION. Thesis.

Lee, S.-G., Lee, H.-S., Lee, J.-S., Choi, G.G. (2015). Shock Response Analysis of Blast Hardened Bulkhead in Naval Ship under Internal Blast. The 2015 World Congress on Advances in Structural Engineering and Mechanics, ISOPE-I-14-611.

Leelachai, M., Benson, S., Dow, R. (2015). Progressive Collapse of Intact and Damaged Stiffened Panels. International Conference on Marine Structures, doi:10.1201/b18179-68.

Li X. (2021). Study on the Damage Effect of Internal Explosive Quasi-Static Pressure Loads to Bulkhead Structures. Ph. D Thesis (In Chinese), North University of China.

Li, C., Dong, S., Wang, T., Xu, W., Zhou, X. (2019). Numerical Investigation on Ultimate Compressive Strength of Welded Stiffened Plates Built by Steel Grades of S235–S390. Applied Sciences 9: 2088, doi:10.3390/app9102088.

Li, L.-M., Zhang, D., Yao, S.J. (2022) Damage Mode Analysis of Steel Box Structures Subjected to Internal Blast Loading. Applied Sciences 12: 10974, doi:10.3390/app122110974.

Li, Z., Zhang, D., Peng, C., Ma, C., Zhang, J., Hu, Z., Zhang, J., Zhao, Y. (2015). The Effect of Local Dents on the Residual Ultimate Strength of 2024-T3 Aluminum Alloy Plate Used in Aircraft under Axial Tension Tests. Engineering Failure Analysis 48: 21–29, doi: 10.1016/j.engfailanal.2014.08.006.

Meng L.P., et al. (2019). Influence of strain rate and stress triaxiality on the dynamic mechanical behavior of Q345B steel. Journal of Ship Mechanics. doi: 10.3969/j.issn.1007-7294.2019.10.007.

Liu, B., Villavicencio, R., Guedes Soares, C. (2013). Experimental and Numerical Plastic Response and Failure of Laterally Impacted Rectangular Plates. Journal of Offshore Mechanics and Arctic Engineering 135: 041602, doi:10.1115/1.4024274.

Mantena, P.R., Cheng, A.H.D., Al-Ostaz, A., Rajendran, A.M. (2010). BLAST AND IMPACT RESISTANT COMPOSITE STRUCTURES FOR NAVY SHIPS. office of naval research – solid mechanics program: marine composites and sandwich structures conference: 379–388.

Martinez, J. L., Cyrino, J. C., Vaz, M. A. (2020). FPSO collision local damage and ultimate longitudinal bending strength analyses. Latin American Journal of Solids and Structures 17(02): e261.

Norman, G. (2024). Yemen's Houthis Kill 2 Sailors in First Fatal Attack on Red Sea Shipping since Hamas Massacre Available online: https://www.foxnews.com/world/yemens-houthis-kill-2-innocent-sailors-first-fatal-attack-red-sea-shipping-hamas-massacre.

Prabowo A R, Bae D M, Cho J H, et al. (2017). Analysis of structural crashworthiness and estimating safety limit accounting for ship collisions on strait territory. Latin American Journal of Solids and Structures, 14(8): 1594-1613.

Menkes, S.B., Opat, H.J. (1973). Tearing and Shear Failures in Explosively Loaded Clamped Beams. Exp. Mech, 13: 480–486.

Yao, S.J., Feipeng, C. (2023). Experimental and Numerical Investigation on the Dynamic Response and Damage of Large-Scale Multi-Box Structure under Internal Blast Loading. Thin-Walled Structures 183: 110430, doi: 10.1016/j.tws.2022.110430.

SMITH, C.S. (1977). Influence of Local Compressive Failure on Ultimate Longitudinal Strength of a Ship's, Hull. Proceedings of the International Symposium on Practical Design in Shipbuilding (PRADS) 73–79.

Smith, M.J., Pegg, N.G. (2003). Automated Assessment of Ultimate Hull Girder Strength. Journal of Offshore Mechanics and Arctic Engineering 125: 211–218, doi:10.1115/1.1577358.

Sun, L., Nie, W., Fu, J. (2006). Plastic Deformation Analysis of a Damaged Ship Under Non-Contact Explosion. Proceedings of the Sixteenth (2006) International Offshore and Polar Engineering Conference 487–490.

U.S. Department of the Army, (1990). the Navy and Air Force. The Design of Structures to Resist the Effects of Accidental Explosions-TechnicalManual (TM 5-1300).

Wang, G., Li, Y., Cui, H., Yang, X., Yang, C., Chen, N. (2021). Acceleration Self-Compensation Mechanism and Experimental Research on Shock Wave Piezoelectric Pressure Sensor. Mechanical Systems and Signal Processing 150: 107303, doi: 10.1016/j.ymssp.2020.107303.

Westine, P.S., Kulesz, J.J., Cox, P.A., Strehlow, R.A., Baker, W.E. (1983). Explosion Hazards and Evaluation.

Wei, W, J., Walters, C.L. (2021). Failure Modes and Rules Related to the Yield-to-Tensile Strength Ratio in Steel Structures. In Proceedings of the Volume 2: Structures, Safety, and Reliability, American Society of Mechanical Engineers: Virtual, Online, June 21 2021, p. V002T02A041.

WU S., ZHANG S., YU H., Li C. (2018). A study of improvement on ultimate bearing capacity of a box girder ship subjected to inner explosion. JOURNAL OF VIBRATION AND SHOCK 37: 50–55, doi: 10.13465/j.cnki.jvs.2018.20.008

Xiong, Z., Li, J., Zhu, H., Liu, X., Liang, Z. (2022). Ultimate bending strength evaluation of MVFT composite girder by using finite element method and machine learning regressors. Latin American Journal of Solids and Structures 19(3): e438.

XU H., ZHANG S., Li C. (2019). Analysis on the Residual Ultimate Strength of Cabin Section After Strength Deck Damage Deformation Due to Non-Contact Explosion. NAVAL ARCHITECTURE AND OCEAN ENGINEERING 35, 18–24, doi: 10.14056/j.cnki.naoe.2019.01.004.

Yu, J., Zhang, L., Pan, J. (2010). Research on the Calculation Method of Explosion Damage Range in Ship Structural Compartments. Proceedings of the 10th National Conference on Impact Dynamics.

Yu, W., Zhao, J., & Shi, J. (2010). Dynamic mechanical behaviour of Q345 steel at elevated temperatures: experimental study. Materials at High Temperatures, 27(4), 285-293, doi.org/10.1007/s40430-020-02628-4.

Zhao, N., Yao, S., Zhang, D., Lu, F., Sun, C. (2020). Experimental and Numerical Studies on the Dynamic Response of Stiffened Plates under Confined Blast Loads. Thin-Walled Structures 154: 106839, doi: 10.1016/j.tws.2020.106839.